

# In Situ $\text{Li}_3\text{PS}_4$ Solid-State Electrolyte Protection Layers for Superior Long-Life and High-Rate Lithium-Metal Anodes

Jianwen Liang, Xiaona Li, Yang Zhao, Lyudmila V. Goncharova, Gongming Wang, Keegan R. Adair, Changhong Wang, Ruying Li, Yongchun Zhu,\* Yitai Qian,\* Li Zhang, Rong Yang, Shigang Lu, and Xueliang Sun\*

A thin and adjustable  $\text{Li}_3\text{PS}_4$  (LPS) solid-state electrolyte protection layer on the surface of Li is proposed to address the dynamic plating/stripping process of Li metal. The LPS interlayer is formed by an in situ and self-limiting reaction between  $\text{P}_4\text{S}_{16}$  and Li in *N*-methyl-2-pyrrolidone. By increasing the concentration of  $\text{P}_4\text{S}_{16}$ , the thickness of the LPS layer can be adjusted up to 60 nm. Due to the high ionic conductivity and low electrochemical activity of  $\text{Li}_3\text{PS}_4$ , the intimate protection layer of LPS can not only prevent the formation of Li dendrites, but also reduces parasitic side reactions and improves the electrochemical performance. As a result, symmetric cells with the LPS protection layer can deliver stable Li plating/stripping for 2000 h. Full cells assembled with the LPS-protected Li exhibit two times higher capacity retention in Li–S batteries ( $\approx 800 \text{ mAh g}^{-1}$ ) at  $5 \text{ A g}^{-1}$  for over 400 cycles compared to their bare Li counterparts. Furthermore, high rate performances can be achieved with Li-LPS/LiCoO<sub>2</sub> cells, which are capable of cycling at rates as high as 20 C. This innovative and scalable approach to stabilizing the Li anode can serve as a basis for the development of next-generation high-performance lithium-metal batteries.

Lithium (Li) is a promising anode for Li–sulfur and Li–air batteries, due to its high theoretical capacity of  $3860 \text{ mAh g}^{-1}$  and low redox potential ( $-3.04 \text{ V}$  vs the standard hydrogen

Dr. J. Liang, Dr. X. Li, Y. Zhao, K. R. Adair, C. Wang, Dr. R. Li, Prof. X. Sun  
Department of Mechanical and Materials Engineering  
University of Western Ontario  
London, Ontario N6A 5B9, Canada  
E-mail: xsun9@uwo.ca

Dr. X. Li, Prof. G. Wang, Dr. Y. Zhu, Prof. Y. Qian  
Hefei National Laboratory for Physical Science at Microscale  
Department of Chemistry  
University of Science and Technology of China  
Hefei, Anhui 230026, P. R. China  
E-mail: yzhu@ustc.edu.cn; ytqian@ustc.edu.cn

Prof. L. V. Goncharova  
Department of Physics and Astronomy  
University of Western Ontario  
London, Ontario N6A 3K7, Canada

Dr. L. Zhang, Dr. R. Yang, Prof. S. Lu  
China Automotive Battery Research Institute  
5th Floor, No. 43, Mining Building, North Sanhuan Middle Road  
Haidian District, Beijing 100088, P. R. China

 The ORCID identification number(s) for the author(s) of this article can be found under <https://doi.org/10.1002/adma.201804684>.

DOI: 10.1002/adma.201804684

electrode), making it the highest energy density anode.<sup>[1–3]</sup> However, several challenges substantially hinder the real application of Li anodes, especially when used in conjunction with organic electrolytes.<sup>[4–6]</sup> As one of the most reactive elements, Li can unavoidably react with organic electrolyte to form a solid electrolyte interphase (SEI) on the surface.<sup>[4]</sup> Secondly, the process of Li plating/stripping only occurs at ion and electron conducting sites, and the nonuniform and low  $\text{Li}^+$  flux of the SEI layer can cause variations in localized current density and ion depletion during cycling, thus resulting in large overpotentials and Li corrosion along with dendrite growth. Continued dendrite growth can lead to penetration of the separator and cause short circuiting of the battery.<sup>[6]</sup> Moreover, nonuniform Li plating/stripping leads to large mechanical deformation and pulverization of the SEI layer, and further parasitic reactions between Li and electrolyte.<sup>[7]</sup> Therefore, the gradual loss of electrolyte and active Li during cycling would result in low Coulombic efficiency and cycling stability.

To this end, various strategies have been proposed to stabilize Li anodes.<sup>[6,8–19]</sup> Previously, 3D conductive current collectors or stable hosts have been utilized to control the Li deposition morphology.<sup>[20–24]</sup> Additionally, ceramic separators with high elastic modulus have been shown to inhibit dendrite formation and penetration.<sup>[16,25,26]</sup> These approaches can be coupled with optimization of the electrolyte through use of additives to improve the stability of the SEI layer during the Li plating/stripping process.<sup>[27–30]</sup> As an alternative strategy, artificial protection layers can reduce the side reactions between Li and electrolyte and are capable of modulating dendrite growth on the electrode surface.<sup>[8–13,31,32]</sup> However, it is still a significant challenge to prevent the unfavorable side reactions between the organic electrolyte and Li due to the large volume change and low  $\text{Li}^+$  flux during high dynamic and long-term Li plating/stripping processes.

Recently, Li et al.<sup>[8]</sup> found that an artificial SEI layer of  $\text{Li}_3\text{PO}_4$  on the surface of Li electrode can restrain the unfavorable reaction between Li metal and organic electrolyte. However, the Li ion conductivity of  $\text{Li}_3\text{PO}_4$  is too low ( $\approx 10^{-9} \text{ S cm}^{-2}$  at  $300 \text{ }^\circ\text{C}$ )<sup>[33]</sup> to further improve their electrochemical performance.

Sulfide-based solid-state electrolyte possess reasonably high ionic conductivity (especially for nanostructured layer, which can achieve ionic conductivities up to  $10 \text{ mS cm}^{-1}$  at room temperature), and is a good choice of materials for the protection of Li metal. Therefore, the formation of a thin solid-state electrolyte layer as isolation layer on the surface of Li metal may address most of the problems of Li anodes in organic electrolyte. Nazar and co-workers<sup>[27]</sup> suggested the formation of LPS on the surface of Li metal based on the use of  $\text{Li}_2\text{S}_6$  and  $\text{P}_2\text{S}_5$  as additives in organic electrolyte, which exhibited excellent cycling performance for symmetric Li cells and  $\text{Li}/\text{Li}_4\text{Ti}_5\text{O}_{12}$  cells. The sulfide-based solid-state electrolyte materials  $\text{Li}_3\text{PS}_4$  is used as an artificial SEI layer due to its high ionic conductivity. Furthermore, the thickness of the sulfide-based solid-state electrolyte layer is very important due to the Li ion flux. Until now, control over the formation of a nanostructured  $\text{Li}_3\text{PS}_4$  layers less than 100 nm has not been achieved.

Here, we provide a new strategy for the synthesis and control over the formation and thickness of  $\text{Li}_3\text{PS}_4$  layer on the surface of Li based on an in situ and self-limiting reaction between  $\text{P}_4\text{S}_{16}$  and Li. The thickness of the  $\text{Li}_3\text{PS}_4$  protection layer can be adjusted up to 60 nm, with changes in the concentration of  $\text{P}_4\text{S}_{16}$  in solution.  $\text{Li}_3\text{PS}_4$  possesses a reasonably high ionic conductivity (especially for nanostructured samples, which can achieve ionic conductivities ranging from  $3 \times 10^{-7}$  to  $1.6 \times 10^{-4} \text{ S cm}^{-1}$  at room temperature<sup>[34,35]</sup>) as a solid-state

electrolyte and the in situ interfacial reaction enables intimate contact between the  $\text{Li}_3\text{PS}_4$  layer and Li metal (Scheme S1a, Supporting Information). The protection layer of  $\text{Li}_3\text{PS}_4$  can not only prevent the formation of Li dendrites but also reduce parasitic side reactions between Li and organic electrolyte and allow uniform and high Li ion flux during the lithium stripping/plating process (Scheme S1b,c, Supporting Information). As a result, symmetric Li-LPS (Li electrode with a protection of  $\text{Li}_3\text{PS}_4$  layer) cells can deliver stable Li plating/stripping voltage profiles for 2000 h with a small voltage hysteresis as low as  $\approx 10 \text{ mV}$ . On the contrary, the bare Li symmetric cell displayed a gradual increase in hysteresis during cycling due to unstable SEI formation, reaching almost 140 mV after 900 h. Moreover, such Li-LPS anodes can further be employed to reshape the electrochemical behavior of Li/S and Li/LiCoO<sub>2</sub> cells at high current density. As examples, a much higher capacity retention of Li-LPS/S cell ( $\approx 800 \text{ mAh g}^{-1}$ ) can be retained at  $5 \text{ A g}^{-1}$  for over 400 cycles, while, bare Li/S cells only offer  $\approx 400 \text{ mAh g}^{-1}$  at the same conditions. Moreover, high rate performances of Li-LPS/LiCoO<sub>2</sub> cell have also been realized when using Li-LPS as anode (9 times higher capacity retention than bare Li/LiCoO<sub>2</sub> cell at 20 C).

Figure 1a shows the in situ fabrication process of the LPS layer on the surface of Li by the reaction between Li and our previously proposed  $\text{P}_4\text{S}_{16}$  molecule.<sup>[36]</sup> To obtain a uniform LPS layer, low moisture and low concentration solution of

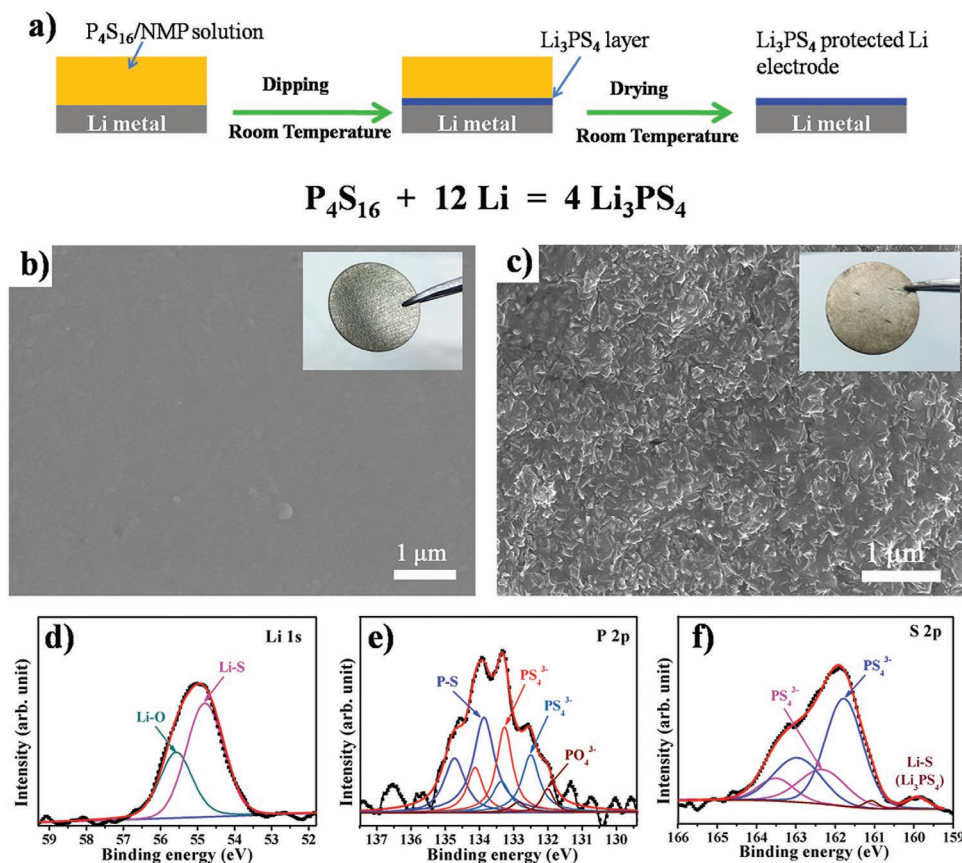


**Figure 1.** Characterization of the Li-LPS-10 electrode. a) Schematic illustration of the in situ formation process of Li-LPS. b,c) SEM images for the surface of the bare Li electrode (b) and the Li-LPS-10 electrode (c). d–f) XPS analysis for the surface of Li-LPS-10.

$P_4S_{16}/NMP$  (*N*-methyl-2-pyrrolidone) is necessary. Moreover, when increasing the concentration of the  $P_4S_{16}/NMP$  solution, the reaction shows a self-limiting process and the thickness of LPS layer could be adjusted up to 60 nm. Detailed synthetic procedures are given in the experimental section. Here, we choose to use one concentration ( $10 \text{ mg mL}^{-1}$ ) of  $P_4S_{16}/NMP$  solution as an example for detailed analysis (marked as Li-LPS-10).

The Li metal is directly used without further treatment (Figures S1 and S2, Supporting Information). At the same time, we also tested the reaction between Li and NMP solvent. Optical image of Li foil after reaction with 2 mL NMP for 24 h at room temperature still remain silvery luster (Figure S3, Supporting Information). The XRD patterns shows a pure Li peak without any impurity (Figure S4, Supporting Information) and the Raman spectrum still shows the same curves with bare Li foil (Figure S5, Supporting Information). Therefore, the reaction between Li and NMP solvent is not serious, which suggests that it can be used as an inert solvent in the in situ fabrication process of the LPS layer. Optical images of bare Li electrode and Li-LPS-10 electrode are shown in the insets of Figure 1b,c and Figure S6 (Supporting Information). Compared to the bare Li electrode, the surface of Li-LPS-10 is obviously covered with a thin and uniform film. Scanning electron microscope (SEM) images of the bare Li electrode demonstrates a smooth and creaseless surface (Figure 1b). After treatment with the  $P_4S_{16}/NMP$  solution ( $10 \text{ mg mL}^{-1}$ ), the resulting Li-LPS-10 electrode has a creased surface layer (Figure 1c). The XRD (X-ray diffraction) pattern of the Li-LPS-10 electrode still reveals the peaks of metallic Li (Figure S7, Supporting Information). Moreover, the distribution of P and S on the surface of LPS layer is uniform based on energy-dispersive X-ray (EDX) elemental mapping (Figure S8, Supporting Information). Detailed cross-sectional SEM images of the Li-LPS electrode are shown in Figure S9 (Supporting Information), on which the thickness of the LPS layer is seen to be uniform and thin.

X-ray photoelectron spectroscopy (XPS) was employed to detect the composition of the LPS layer. Figure 1d–f shows the Li 1s, S 2p, and P 2p XPS spectra of the Li-LPS-10 electrode. The XPS spectrum of the Li 1s can be fitted by two Gaussian component peaks at 54.8 and 55.6 eV (Figure 1d). The peak at 54.8 eV can be assigned to Li–S bonding<sup>[37,38]</sup> and the peak at 55.6 eV is related to the Li–O bond.<sup>[39,40]</sup> No characteristic peaks of Li metal (53.1 eV)<sup>[41]</sup> is found. Moreover, the P 2p spectrum exhibits several peaks, which can be fitted with four distinct doublets ( $2p_{1/2}$  and  $2p_{3/2}$ ) (Figure 1e). Among them, a special double peaks of the P  $2p_{3/2}$  appear at 133.3 and 132.5 eV can be assigned to  $PS_4^{3-}$ , while the S 2p spectrum confirmed the proper assignment with the responsive peaks of S  $2p_{3/2}$  at 162.5 and 161.6 eV (Figure 1f).<sup>[42]</sup> The peak of P  $2p$  spectrum at 132.1 eV (P  $2p_{3/2}$ ) originates from  $PO_4^{3-}$ ,<sup>[43]</sup> which is due to the unavoidable oxidation during the XPS preparation and transfer process. Except for the peaks of  $PS_4^{3-}$ , there is a special peak of P  $2p$  spectrum at 133.9 eV (P  $2p_{3/2}$ ), which is related to the bond of P–S.<sup>[42]</sup> Moreover, Raman spectrum of Li-LPS-10 foil (Figure S10, Supporting Information) demonstrated three typical peaks between 300 and  $1000 \text{ cm}^{-1}$ . The peak located at  $442 \text{ cm}^{-1}$  is related to  $Li_3PS_4$  and the peak at  $521 \text{ cm}^{-1}$  can be assigned to  $Li_2O$ . There is a wide peak located at  $\approx 950 \text{ cm}^{-1}$ , which is related to the signal of  $PO_4^{3-}$ . The existent of  $Li_2O$

and  $PO_4^{3-}$  maybe due to the unavoidable oxidation during the Raman preparation, transfer and testing process. Therefore, combined with the information obtained from Raman, XPS spectra and our previous result on the detail lithiation mechanism of  $P_4S_{16}$  cathode,<sup>[36]</sup> it can be further concluded that  $Li_3PS_4$  is the main product in the reaction between  $P_4S_{16}$  and metallic Li.

Moreover, Rutherford Backscattering Spectrometry (RBS) were performed to further show the thickness of the prepared LPS layer. Figures S11 and 12 (Supporting Information) demonstrate the RBS spectra and simulation profiles on the Li-LPS-10 electrode. From the figure, it can be found that Li, P, and S peaks are clearly visible. Moreover, a strong O peak and a weak C peak have been found, which is related to the air exposure of the Li-LPS-10 electrode during the transfer process. From the integrated area density of Li, P, and S peaks, we can estimate that an  $\approx 60 \text{ nm}$  thick LPS layer has been formed. Moreover, in order to control the thickness of the LPS layer, we try to change the concentration of  $P_4S_{16}/NMP$  solution from 1 to  $15 \text{ mg mL}^{-1}$ . RBS testing of Li-LPS-1 shows that the thickness of the LPS layer is about 32 nm (Figures S13 and 14, Supporting Information). Furthermore, when the concentration is increase to  $2.5 \text{ mg mL}^{-1}$ , the thickness of the LPS layer is increased to  $\approx 60 \text{ nm}$  (Figures S15 and S16, Supporting Information). This result is similar to the thickness of Li-LPS-10, indicating that the reaction between Li and  $P_4S_{16}$  follows a self-limiting process and the LPS layer can be adjusted up to  $\approx 60 \text{ nm}$ .

Galvanostatic Li plating/stripping was carried out by using coin cells to substantiate the stability of the Li-LPS electrode. CR2016 coin cells were assembled as bare Li or Li-LPS electrode symmetric cells. The Nyquist plots of the symmetric Li/Li and Li-LPS-10/Li-LPS-10 cells after assembling were tested by electrochemical impedance spectroscopy (EIS). As shown in Figure S17 (Supporting Information), the impedance of the cell is slightly increased from the initial standing process to  $\approx 20 \text{ h}$ . The increase of impedance during the standing process is related to the SEI formation from the side reactions between Li and ether based electrolyte. The Nyquist plots of the symmetric Li-LPS/Li-LPS cells exhibit different behaviors as shown in Figure S18 (Supporting Information). The impedance of the cell is much more stable and even a slight decrease can be found during the standing process from 0 to 24 h. **Figure 2a–c** and Figure S19–S28 (Supporting Information) compare the voltage profiles of bare Li and Li-LPS symmetric cells cycled at  $0.5 \text{ mA cm}^{-2}$  and  $1 \text{ mAh cm}^{-2}$  capacity. The bare Li symmetric cell (Figure 2b,c) displayed a gradual increase in hysteresis during cycling, reaching 23 mV after 500 h and up to 140 mV after 900 h. The continuous increase in overpotential is likely due to an unstable SEI formation during cycling. Compared to the bare Li symmetrical cell, the Li-LPS cells show a significant improvement in cycling stability. For the symmetric Li-LPS-1 cell (Figures S19 and S20, Supporting Information), a small increase of voltage hysteresis during long term cycling is observed, indicating that a 32 nm thick LPS layer is still not enough to increase the stability of Li metal. When increasing the thickness of the LPS protection layer to 60 nm (Li-LPS-2 to Li-LPS-15), the voltage hysteresis of the Li-LPS symmetric cell is stable without obvious fluctuation for long term cycling

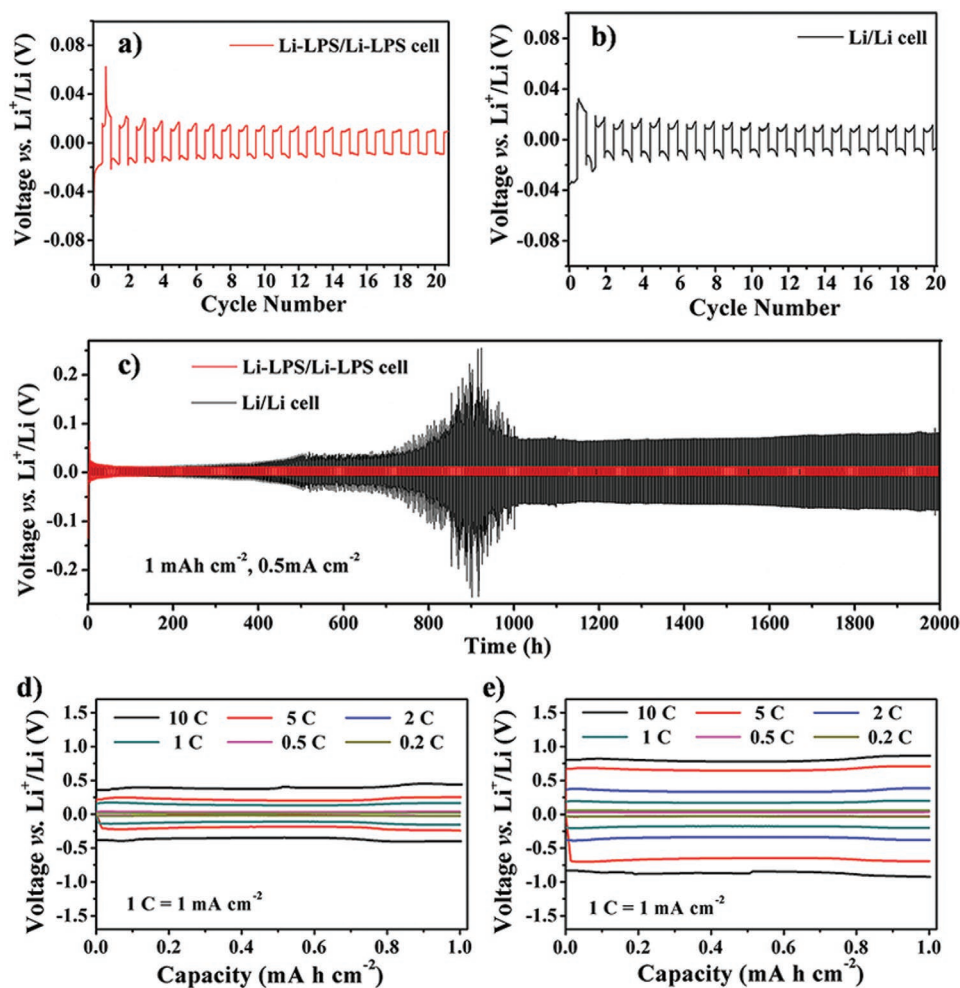


**Figure 2.** Electrochemical characterizations of the Li-LPS-10 and bare Li electrodes. a,b) Charge/discharge curves of the Li-LPS-10 and bare Li symmetric cell. c) Long-term cycling performance of Li and Li-LPS-10 symmetric cells. d,e) Voltage profiles of Li-LPS-10 and bare Li symmetric cell at different current density.

(Figures S21–S28, Supporting Information). As an example, the symmetric Li-LPS-10 cell delivered stable Li plating/stripping voltage profiles for up to 2000 h with stable voltage hysteresis ( $\approx 10$  mV, Figure 2c). Moreover, to further study the evolution of the hysteresis in detail, the 5th (16–20 h), 50th (196–200 h), 100th (396–400 h), 150th (596–600 h), 200th (796–800 h), and 250th (996–1000 h) cycle of the Li-LPS-10 and bare Li symmetric cells were enlarged in Figure S29 (Supporting Information). For the Li-LPS-10 symmetric cell, except for the initial fifteen cycles, flat and overlapped voltage plateaus ( $\approx 10$  mV for charging and  $\approx -10$  mV for discharging) can be retained during cycling without any significant increase/decrease in hysteresis. Beyond 2000 h, as shown in Figure 2c, the Li-LPS-10 cell still revealed outstanding cycling stability and low voltage hysteresis. For bare Li, the voltage plateau for the charging process of 5th, 50th, 100th, 150th, 200th and 250th cycle is 8, 8, 10, 25, 50, and 90 mV, respectively. Compared to the Li-LPS-10 cell, the bare Li cell showed higher overpotential at each plating/stripping process and a gradual increase of voltage hysteresis during cycling. Except the gradual increase in voltage hysteresis, the bare Li electrode also exhibited several fluctuating

voltage profiles. As exemplified from  $\approx 800$  to 1000 h, the voltage curves tend to fluctuate with sudden voltage drops, indicating an internal soft short-circuit due to Li dendrite formation. After 1000 h, the bare Li cell changed to a stable hysteresis voltage, which is related to the formation of thick SEI layer.

Moreover, the Li plating/stripping profiles of bare Li and Li-LPS-10 symmetric cells at different current densities are shown in Figure 2d,e and Figure S30 (Supporting Information). The voltage hysteresis is characteristic of the electrochemical dynamics of Li plating/stripping. At  $0.5 \text{ mA cm}^{-2}$ , the voltage hysteresis for the Li-LPS-10 electrode is  $\approx 30$  mV, whereas that of the bare Li electrode is  $\approx 35$  mV. When the current density is increased to 1, 2, 5, and  $10 \text{ mA cm}^{-2}$ , the average voltage hysteresis for the Li-LPS-10 electrode is  $\approx 80, 130, 210,$  and  $400$  mV, respectively. For bare Li, the voltage hysteresis in the Li plating/stripping increases gradually as the current density increases, with a typical average hysteresis of  $\approx 170, 350, 650,$  and  $860$  mV at 1, 2, 5, and  $10 \text{ mA cm}^{-2}$ , respectively. As evidenced by galvanostatic cycling, the voltage hysteresis of Li-LPS-10 is significantly lower than that of the bare Li electrode at high current density, highlighting the ability of the LPS protection layer to

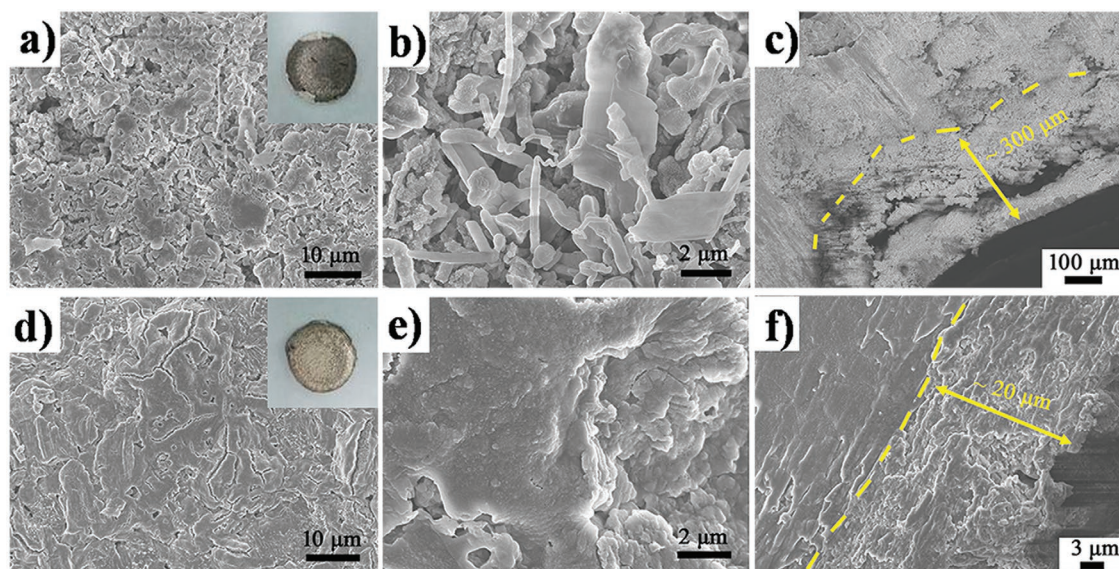


**Figure 3.** Characterization of bare Li and Li-LPS electrodes after 200 cycles at  $1 \text{ mA cm}^{-2}$  for  $1 \text{ mAh cm}^{-2}$ . a,b) Top-view and c) cross-sectional SEM images of bare Li electrode after cycling. d,e) Top-view and f) cross-sectional SEM images of the Li-LPS electrode after cycling.

stabilize the SEI and provide a higher ionic conductivity compared to the bare Li.

The reduced voltage hysteresis of Li-LPS-10 can be further supported by EIS. The corresponding Nyquist plots of the bare Li and Li-LPS-10 symmetric cells are shown in Figure S31 (Supporting Information). The semi-circle at the high-frequency range of Nyquist plot is related to the diffusion resistance of  $\text{Li}^+$ /electron through the interface layer between Li and electrolyte. The bare Li symmetric cell displays a large interfacial resistance ( $R_i$ ) of  $\approx 170 \Omega$  before cycling, which is due to the native SEI layers formed on the surface of the Li through the reactions between Li and electrolyte. After 10 cycles,  $R_i$  dropped to a lower value of  $\approx 80 \Omega$  due to the morphological change of the SEI layer and possible dendrite formation, which significantly increases the contact area between Li and electrolyte. In contrast, the Li-LPS-10 symmetric cell has a low initial  $R_i$  of  $\approx 70$  and  $\approx 60 \Omega$  after 10 cycles. This phenomenon can illustrate the improved stability and stripping/plating kinetics of the Li-LPS-10 electrode. Thus, the Li-LPS-10 electrode can reveal a significantly reduced voltage hysteresis during Li stripping/plating. In addition, the Li-LPS-10 electrode can also retain a delithiation capacity near the theoretical value of Li. As shown in Figure S32 (Supporting Information), a delithiated capacity of  $\approx 3540 \text{ mAh g}^{-1}$  (based on the whole mass of Li-LPS-10 electrode) can be achieved when charged to  $1.0 \text{ V}$  (vs  $\text{Li}/\text{Li}^+$ ). The high specific delithiation capacity can be attributed to the nanoscale thickness and light weight of the LPS protection layer. Therefore, the protective LPS coating of the Li electrode offers the exciting possibility of fabricating high performance Li electrode with a minimal effect on capacity.

In order to reveal the underlying mechanism of the improved electrochemical performances, we further observe the morphological evolution of the Li electrode with and without a LPS protection layer after cycling. To analyze the surface of the electrodes, Li and Li-LPS-10 symmetric cells cycled at  $0.5 \text{ mA cm}^{-2}$  for 200 cycles were disassembled in a glove

box for SEM analysis. The changes in surface morphology of the Li and Li-LPS electrodes are shown in Figure 3. For the bare Li electrode, a thick, fragile and gray layer was found on the surface (Figure 3a, inset). Furthermore, compared to the pristine Li, the surface of the Li electrode becomes rough after cycling (Figure 3a). The SEM images reveal that there are large amounts of loose, porous and dendritic structures with a thickness up to  $\approx 300 \mu\text{m}$  (Figure 3b,c). The dendrite structures on the surface of the Li exhibits a diameter of  $\approx 1 \mu\text{m}$  and lengths of up to tens of micrometers. In comparison with the bare Li electrode, the overall morphology of Li-LPS electrode is smoother, without obvious Li dendrite formation after 200 cycles (Figure 3d,e). The photo of Li-LPS-10 electrode from the disassembled symmetric cell after cycling still demonstrated a smooth surface, which without the existent of fragile and gray surface layer (Figure 3d, inset). Moreover, the corrosion of Li-LPS electrode is obviously reduced ( $\approx 20 \mu\text{m}$ ) compared to that of the bare Li electrode after cycling (Figure 3f). Thus, it can be concluded that the existence of a LPS protection layer on the surface of Li can prevent the formation of Li dendrites, reduce the decomposition of electrolyte, stabilize the SEI, and prevent further corrosion of Li metal during battery cycling.

Moreover, analysis of the SEI layer composition for Li and Li-LPS-10 electrodes after 200 cycles was carried out by XPS. The obtained results are presented in Figure 4 and Figures S33 and S34 (Supporting Information). In the XPS survey spectra, peaks located at  $\approx 53.8, 166.9, 284.8, 398.8, 530.8,$  and  $688.4 \text{ eV}$  were observed in both samples, corresponding to Li 1s, S 2p, C 1s, N 1s, O 1s, and F 1s, respectively (Figure S33, Supporting Information).<sup>[44,45]</sup> As for the Li-LPS electrode after cycling, four distinct doublets ( $2p_{1/2}$  and  $2p_{3/2}$ ) of the P 2p spectra can be found (Figure 4a), which are similar to that of the Li-LPS electrode before cycling. The responsive peaks of P  $2p_{3/2}$  at  $133.4$  and  $132.7 \text{ eV}$  corresponding to the existence of  $\text{PS}_4^{3-}$  on the surface of Li-LPS after cycling, while the S 2p spectrum validates the assignment with a response measured at  $161.6 \text{ eV}$

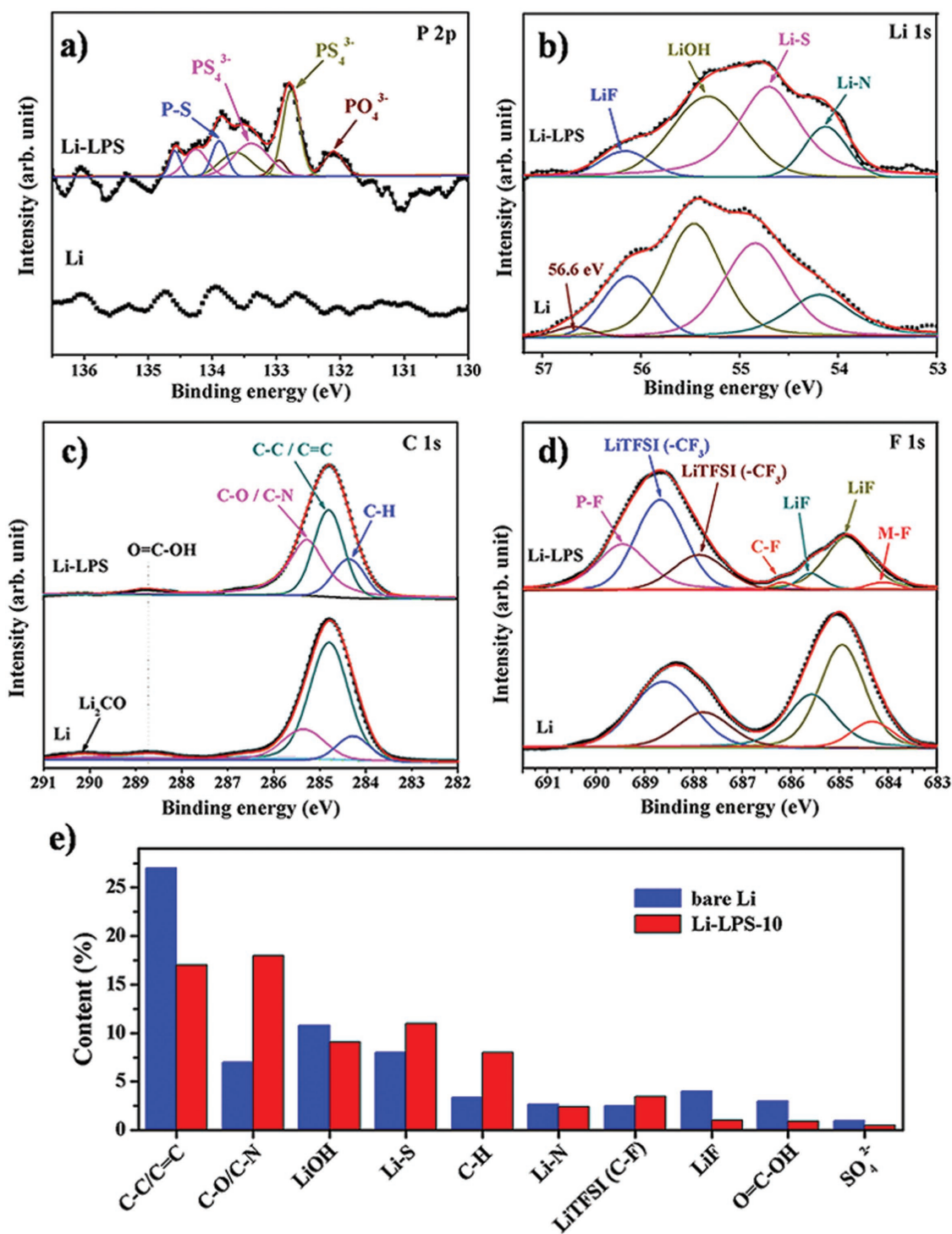


**Figure 4.** a) P 2p, b) Li 1s, c) F 1s, and d) C 1s XPS spectra and their fitted curves for the surface chemical composition of SEI layer of Li and Li-LPS-10 electrode after 200 cycles. e) The main degradation products and these related contents in SEI layer of Li and Li-LPS-10 electrode after 200 cycles.

see the Appendix and Figure S34 in the Supporting Information.<sup>[42]</sup> These two peaks are similar to the pristine Li-LPS-10 electrode. Thus, it can be concluded that  $Li_3PS_4$  still exists on the surface of Li, which further provides evidence of the flexibility of the  $Li_3PS_4$  protection layer. In addition, the Li 1s spectrum obtained from both electrodes contain several Li peaks at 56.1, 55.3, 54.8 and

54.2 eV (Figure 4b). The peak at 56.1 eV suggested the presence of LiF.<sup>[17,46]</sup> The peak at 55.3 eV is attributed not only to LiOH but also to  $Li_2CO_3$  or  $Li-CO_2R$  organic species.<sup>[17,42]</sup> The peak at 54.8 eV is related to the Li-S bond<sup>[37,38]</sup> and the peak at 54.2 eV originates from the Li-N bond.<sup>[47,48]</sup> Table S1 (Supporting Information) shows all of the peaks and the related

assignments, contents and references. From the table, it can be found that the content of LiF (calculated from Li 1s spectrum) in the bare Li electrode after cycling is 16.4 at%, which is much higher than that of Li-LPS electrode after cycling (6 at%). The F 1s spectrum also suggests a much higher content of LiF (at the peaks of 685.5 and 684.8 eV)<sup>[46,49]</sup> in Li electrode after cycling than Li-LPS electrode (Figure 4c). The LiF content of Li-electrode after cycling for F 1s spectrum is about 61.0 at%, while the LiF content of Li-LPS electrode after cycling is only about 24.2 at%. In addition to the presence of LiF, the F 1s spectrum also suggests the presence of LiTFSI and LiSO<sub>2</sub>F with a band at 688.5 and 687.8 eV, associated with the peak of S 2p spectrum at 169.5 eV (S 2p<sub>3/2</sub>, Figure S34, Supporting Information).<sup>[17]</sup> Moreover, compared to the F 1s spectrum of Li electrode after cycling, an additional peak of P–F (689.2 eV)<sup>[17]</sup> is present on the SEI surface of the Li-LPS-10 electrode. For the C 1s spectrum (Figure 4d), except for the typical peaks of 284.3 eV (C–H),<sup>[50,51]</sup> 284.8 eV (C–C)<sup>[44,50]</sup> and 285.3 eV (C–O or C–N),<sup>[17,50]</sup> a new peak of 290.2 eV (assigned to CO<sub>3</sub><sup>2-</sup>)<sup>[17]</sup> and a higher intensity peak of 288.7 eV (assigned to O=C–OH)<sup>[52]</sup> have been found in the SEI, which indicates a higher degree of SEI degradation in the bare Li electrode compared to that of the Li-LPS counterpart.

The degradation products and related contents of the SEI layers of Li and Li-LPS-10 electrodes after cycling is summarized in Figure 4e and Table S1 (Supporting Information). When compared to Bare Li after cycling, the concentration of LiF, CO<sub>3</sub><sup>2-</sup>, –SO<sub>2</sub>F, O=C–OH species, etc., in the SEI layer of Li-LPS electrode is decreased. Thus, the LPS protection layer

can reduce degradation of inorganic products and slow down the degree of electrolyte consumption during cycling. Moreover, the peaks of PS<sub>4</sub><sup>3-</sup> still can be detected in Li-LPS-10 after long-term cycling, suggesting that the Li<sub>3</sub>PS<sub>4</sub> layer is a stable and flexible coating. On the other hand, Raman spectra of Li-LPS-10 electrode after cycling still exhibited the same peaks observed in the pristine Li-LPS electrode, which provides further evidence of the stability of the protection layer (Figure S35, Supporting Information).

To test the performance of the LPS protection layer in real application, full cells were fabricated and paired with S@C and lithium cobalt oxide (LCO) cathodes. Until now, Li/S cells displayed significant issues related to the shuttle effect, where long chain polysulfides diffuse to the surface of the lithium anode and are reduced to short chain polysulfides during standing and discharging processes. The short chain polysulfides can then move back to the cathode and be oxidized to long-chain polysulfides or sulfur. This parasitic process takes place continuously, creating an internal “shuttle” phenomenon.<sup>[53]</sup> It decreases the active mass utilization in the discharge process, markedly reduces the Coulombic efficiency and degrades the cycling life. Therefore, the protection layer of LPS on the surface of Li should not only improve the electrochemical performance of Li anode but also can block the side reactions between soluble long-chain polysulfide and Li, leading to a reduction in the shuttle effect of polysulfides when using S as a cathode. Subsequently, a high initial discharge capacity and improved cycling performance can be achieved based on the LPS protection layer. As shown in Figure 5, the LPS/S cell exhibits an

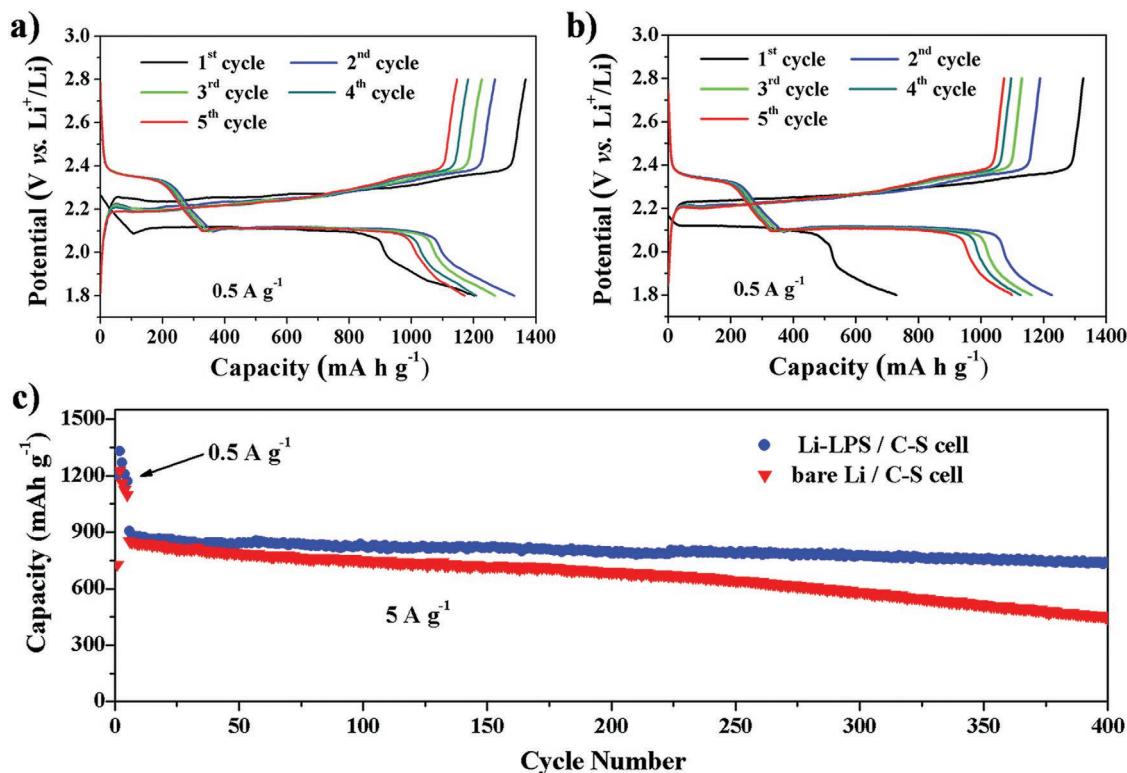


**Figure 5.** Electrochemical performance of Li-LPS/S and Li/S cells. a,b) Galvanostatic charge/discharge curves of the Li-LPS/S cell (a) and the Li/S cell (b). c) Cycling performance of the Li-LPS/S and Li/S cells.

initial capacity of 1.7 times higher than the Li/S cell at 0.5 A g<sup>-1</sup> (≈1200 mAh g<sup>-1</sup> vs 720 mAh g<sup>-1</sup>). The significant differences between the bare Li/S and Li-LPS/S cell in the length of the voltage plateau of initial discharge process is related to different degree of self-discharging. Based on this, it can be found that the LPS protection layer can effectively reduce the self-discharging phenomenon of Li/S cell. Moreover, the Li-S cells with LPS protection layer exhibited a much higher capacity (≈800 mAh g<sup>-1</sup>) at a high current density of 5 A g<sup>-1</sup> for over 400 cycles. In contrast, the bare Li cells only offer ≈400 mAh g<sup>-1</sup> after 400 cycles at the same charge/discharge rate. From the voltage profiles of initial five cycles (Figure 5a,b) and 50th, 100th, 200th, 300th, 400th cycles in Figure S36 (Supporting Information), it can be seen that the charge/discharge curves of Li-LPS/S cell is much more stable. Moreover, the Coulombic efficiency of the Li-LPS cell can achieve an average value of 96% after 400 cycles, while the Coulombic efficiency of the cell with bare Li is reduced to an average efficiency of 89% after 400 cycles (Figure S37, Supporting Information). This demonstrates the improved reversibility and stability of Li-LPS for Li-S batteries. We believe that the good performance of the LPS/S cell is attributed to the greatly reduced shuttle effect because of the LPS protection layer.

On the other hand, when using LCO as the cathode, the Li-LPS/LCO cells reveal a significantly improved rate performance and reversible capacity compared to that of the Li/LCO cell (Figure 6). Figure 6 compares the rate performance of Li-LPS/LCO and Li/LCO cells at different current densities. The Li-LPS/LCO cell can be seen to exhibit

an average reversible capacity of ≈137, 136, 132, 120, and 104 mAh g<sup>-1</sup> at 0.5, 1, 2, 5, and 10 C, respectively. Even at a high current density of 20 C, a reversible capacity of 70 mAh g<sup>-1</sup> can still be achieved. When the current density is returned back to 1 C, the Li-LPS/LCO cell can still retain a capacity of 137 mAh g<sup>-1</sup>. In contrast, the Li/LCO cell reveals average reversible capacities of 137, 124, 114, 92, 57, and 8 mAh g<sup>-1</sup> at 0.5, 1, 2, 5, 10, and 20 C, respectively. It can be concluded that the rate capability of the Li-LPS/LCO cell is significantly higher than that of the Li/LCO cell, especially when cycled at ultra-high current densities. The high rate performance of Li-LPS/LCO cell is likely to originate from the high-speed Li<sup>+</sup> migration from the electrolyte to the Li electrode under the assistance of the LPS protection layer. Moreover, the Li<sub>3</sub>PS<sub>4</sub>-modified Li-metal electrode after cycling in a Li-LPS/LCO cell exhibits more uniform and smooth surface than bare Li electrode after cycling without LPS protection (Figure S38, Supporting Information).

In summary, we designed an LPS solid-state electrolyte protection layer that is capable of stabilizing Li anodes. Based on the high ionic conductivity and low electrochemical activity of Li<sub>3</sub>PS<sub>4</sub>, the LPS protection layer can not only limit the unfavorable reaction between Li and organic electrolyte and enable uniform Li ion flux but can also stabilize the SEI layer and suppress Li dendrite growth. Thus, stabilized Li anodes with long-term cycling and high rate performance have been achieved in symmetrical cells, Li-S cells, and Li-LiCoO<sub>2</sub> batteries.

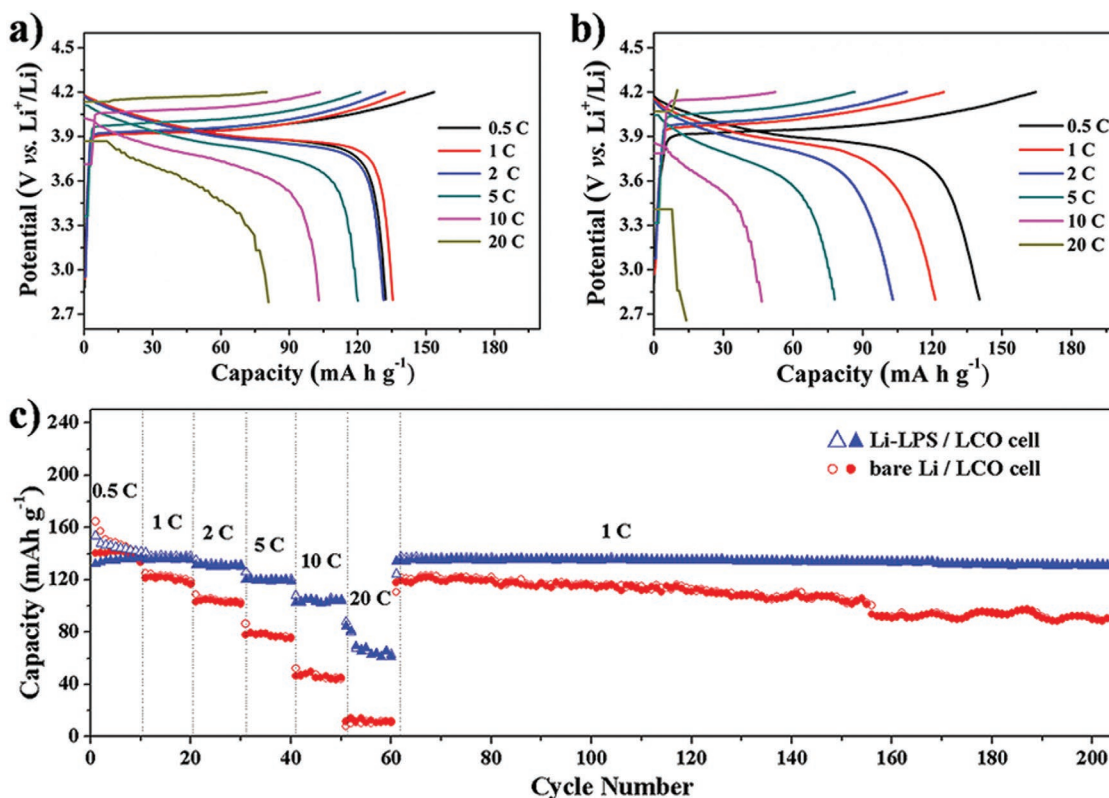


**Figure 6.** Electrochemical performance of Li-LPS/LiCoO<sub>2</sub> and Li/LiCoO<sub>2</sub> cells. a,b) Galvanostatic charge/discharge curves of the Li-LPS/LiCoO<sub>2</sub> cell (a) and the Li/LiCoO<sub>2</sub> cell (b). c) Cycling and rate performance of the Li-LPS/LiCoO<sub>2</sub> and Li/LiCoO<sub>2</sub> cells.

## Supporting Information

Supporting Information is available from the Wiley Online Library or from the author.

## Acknowledgements

This work was supported by the National Key Research and Development Program of China (Nos. 2017YFA0206702 and 2017YFA0206703), the National Natural Science Foundation of China (Nos. 21521001, 51602303, and 21671183), the China Postdoctoral Science Foundation (2016T90626 and 2016T90581), the Natural Science and Engineering Research Council of Canada (NSERC), the Canada Research Chair Program (CRC), the Ontario Research Fund, the Canada Foundation for Innovation (CFI), the China Automotive Battery Research Institute Co., and the University of Western Ontario.

## Conflict of Interest

The authors declare no conflict of interest.

## Keywords

Li<sub>3</sub>PS<sub>4</sub>, lithium batteries, lithium-metal anodes, solid-state electrolytes, surface isolation layer

Received: July 21, 2018

Revised: August 25, 2018

Published online: October 1, 2018

- [1] X. Fang, H. Peng, *Small* **2015**, *11*, 1488.
- [2] D. Lin, Y. Liu, Y. Cui, *Nat. Nanotechnol.* **2017**, *12*, 194.
- [3] W. Xu, J. Wang, F. Ding, X. Chen, E. Nasybulin, Y. Zhang, J. Zhang, *Energy Environ. Sci.* **2014**, *7*, 513.
- [4] G. Zheng, S. Lee, Z. Liang, H. Lee, K. Yan, H. Yao, H. Wang, W. Li, S. Chu, Y. Cui, *Nat. Nanotechnol.* **2014**, *9*, 618.
- [5] M. Tikekar, S. Choudhury, Z. Tu, L. Archer, *Nat. Energy* **2016**, *1*, 16114.
- [6] X. Cheng, T. Hou, R. Zhang, H. Peng, C. Zhao, J. Huang, Q. Zhang, *Adv. Mater.* **2016**, *28*, 2888.
- [7] W. Liu, D. Lin, A. Pei, Y. Cui, *J. Am. Chem. Soc.* **2016**, *138*, 15443.
- [8] N. Li, Y. Yin, C. Yang, Y. Guo, *Adv. Mater.* **2016**, *28*, 1853.
- [9] B. Zhu, Y. Jin, X. Hu, Q. Zheng, S. Zhang, Q. Wang, J. Zhu, *Adv. Mater.* **2017**, *29*, 1603755.
- [10] A. Kozen, C. Lin, A. Pearce, M. Schroeder, X. Han, L. Hu, S. Lee, G. Rubloff, M. Noked, *ACS Nano* **2015**, *9*, 5884.
- [11] Y. Liu, D. Lin, P. Yan, Y. Liu, J. Xie, R. Dauskardt, Y. Cui, *Adv. Mater.* **2017**, *29*, 1605531.
- [12] E. Kazyak, K. Wood, N. Dasgupta, *Chem. Mater.* **2015**, *27*, 6457.
- [13] K. Liu, A. Pei, H. Lee, B. Kong, N. Liu, D. Lin, Y. Liu, C. Liu, P. Hsu, Z. Bao, Y. Cui, *J. Am. Chem. Soc.* **2017**, *139*, 4815.
- [14] L. Ma, M. Kim, L. Archer, *Chem. Mater.* **2017**, *29*, 4181.
- [15] X. Cheng, C. Yan, X. Zhang, H. Liu, Q. Zhang, *ACS Energy Lett.* **2018**, *3*, 1564.
- [16] W. Zhou, S. Wang, Y. Li, S. Xin, A. Manthiram, J. Goodenough, *J. Am. Chem. Soc.* **2016**, *138*, 9385.
- [17] A. Basile, A. Bhatt, A. O'Mullane, *Nat. Commun.* **2016**, *7*, ncomms11794.
- [18] Z. Hu, S. Zhang, S. Dong, W. Li, H. Li, G. Cui, L. Chen, *Chem. Mater.* **2017**, *29*, 4682.
- [19] J. Qian, W. Xu, P. Bhattacharya, M. Engelhard, W. Henderson, Y. Zhang, J. Zhang, *Nano Energy* **2015**, *15*, 135.
- [20] D. Lin, Y. Liu, Z. Liang, H. Lee, J. Sun, H. Wang, K. Yan, J. Xie, Y. Cui, *Nat. Nanotechnol.* **2016**, *11*, 626.
- [21] J. Kim, D. Kim, H. Jung, J. Choi, *Chem. Mater.* **2015**, *27*, 2780.
- [22] Z. Liang, D. Lin, J. Zhao, Z. Lu, Y. Liu, C. Liu, Y. Lu, H. Wang, K. Yan, X. Tao, *Proc. Natl. Acad. Sci. USA* **2016**, *113*, 2862.
- [23] X. Cheng, H. Peng, J. Huang, R. Zhang, C. Zhao, Q. Zhang, *ACS Nano* **2015**, *9*, 6373.
- [24] H. Ye, S. Xin, Y. Yin, J. Li, Y. Guo, L. Wan, *J. Am. Chem. Soc.* **2017**, *139*, 5816.
- [25] W. Luo, L. Zhou, K. Fu, Z. Yang, J. Wan, M. Manno, Y. Yao, H. Zhu, B. Yang, L. Hu, *Nano Lett.* **2015**, *15*, 6149.
- [26] K. Fu, Y. Gong, J. Dai, A. Gong, X. Han, Y. Yao, C. Wang, Y. Wang, Y. Chen, C. Yan, *Proc. Natl. Acad. Sci. USA* **2016**, *113*, 7094.
- [27] Q. Pang, X. Liang, A. Shyamsunder, L. Nazar, *Joule* **2017**, *1*, 871.
- [28] J. Qian, W. Henderson, W. Xu, *Nat. Commun.* **2015**, *6*, 6362.
- [29] Y. Lu, Z. Tu, L. Archer, *Nat. Mater.* **2014**, *13*, 961.
- [30] X. Cheng, M. Zhao, C. Chen, A. Pentecost, K. Maleski, T. Mathis, X. Zhang, Q. Zhang, J. Jiang, Y. Gogotsi, *Nat. Commun.* **2017**, *8*, 336.
- [31] J. Xie, L. Liao, Y. Gong, Y. Gong, Y. Li, F. Shi, A. Pei, J. Sun, R. Zhang, B. Kong, R. Subbaraman, J. Christensen, Y. Cui, *Sci. Adv.* **2017**, *3*, eaao3170.
- [32] H. Wu, Y. Cao, L. Geng, C. Wang, *Chem. Mater.* **2017**, *29*, 3572.
- [33] M. Touboul, N. Sephar, M. Quarton, *Solid State Ionics* **1990**, *38*, 225.
- [34] Z. Liu, W. Fu, E. Payzant, X. Yu, Z. Wu, N. Dudney, J. Kiggans, K. Hong, A. Rondinone, C. Liang, *J. Am. Chem. Soc.* **2013**, *135*, 975.
- [35] Z. Quan, M. Hirayama, D. Sato, Y. Zheng, T. Yano, K. Hara, K. Suzuki, M. Hara, R. Kanno, *J. Am. Ceram. Soc.* **2017**, *100*, 746.
- [36] X. Li, J. Liang, Y. Lu, Z. Hou, Q. Cheng, Y. Zhu, Y. Qian, *Angew. Chem., Int. Ed.* **2017**, *56*, 2937.
- [37] J. Kim, T. Kim, Y. Jeong, K. Lee, K. Park, S. Yang, C. Park, *Adv. Energy Mater.* **2015**, *5*, 1500268.
- [38] V. Atuchin, L. Isaenko, V. Kesler, S. Lobanov, *J. Alloys Compd.* **2010**, *497*, 244.
- [39] B. Chowdari, G. Subba Rao, G. Lee, *Solid State Ionics* **2000**, *136–137*, 1067.
- [40] Y. Chu, Z. Fu, Q. Qin, *Electrochim. Acta* **2004**, *49*, 4915.
- [41] S. Xiong, K. Xie, Y. Diao, X. Hong, *J. Power Sources* **2014**, *246*, 840.
- [42] C. Zu, M. Klein, A. Manthiram, *J. Phys. Chem. Lett.* **2014**, *5*, 3986.
- [43] X. Cui, Q. Li, Y. Li, F. Wang, G. Jin, M. Ding, *Appl. Surf. Sci.* **2008**, *255*, 2098.
- [44] Y. Shulga, T. Tien, C. Huang, S. Lo, V. Muradyan, N. Polyakova, Y. Ling, R. outfy, A. Moravsky, *J. Electron Spectrosc. Relat. Phenom.* **2007**, *160*, 22.
- [45] C. Zeng, F. Xie, X. Yang, M. Jaroniec, L. Zhang, S. Qiao, *Angew. Chem., Int. Ed.* **2018**, *57*, 8540.
- [46] S. Leroy, F. Blanchard, R. Dedryvere, H. Martinez, B. Carré, D. Lemordant, D. Gonbeau, *Surf. Interface Anal.* **2005**, *37*, 773.
- [47] J. Yang, Y. Jia, Z. Yao, *Solid State Ionics* **1997**, *96*, 215.
- [48] A. Arof, N. Morni, M. Yarmo, *Mater. Sci. Eng., B* **1998**, *55*, 130.
- [49] H. Ota, T. Sato, H. Suzuki, T. Usami, *J. Power Sources* **2001**, *97–98*, 107.
- [50] H. Cheng, C. Zhu, M. Lu, Y. Yang, *J. Power Sources* **2007**, *173*, 531.
- [51] R. Dedryvere, S. Leroy, H. Martinez, F. Blanchard, D. Lemordant, D. Gonbeau, *J. Phys. Chem. B* **2006**, *110*, 12986.
- [52] K. Zhang, Y. Xu, Y. Lu, Y. Zhu, Y. Qian, D. Wang, J. Zhou, N. Lin, Y. Qian, *J. Mater. Chem. A* **2016**, *4*, 6404.
- [53] C. Ye, L. Zhang, C. Guo, D. Li, A. Vasileff, H. Wang, S. Qiao, *Adv. Funct. Mater.* **2017**, *27*, 1702524.